RSC Advances




ROYAL SOCIETY OF CHEMISTRY

www.rsc.org/advances

**TOC**

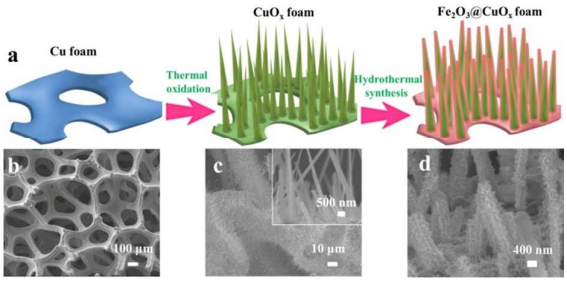


A high-performance monolith catalyst based on 3D hierarchical foam-like $Fe_2O_3$@$CuO_x$ was developed for selective catalytic reduction of NO.

Journal Name RSCPublishing

ARTICLE

# Rational design of 3D hierarchical foam-like $Fe_2O_3$@CuOx monolith catalysts for selective catalytic reduction of NO with $NH_3$

Cite this: DOI: 10.1039/x0xx00000x

Received 00th January 2012,
Accepted 00th January 2012

DOI: 10.1039/x0xx00000x

www.rsc.org/

Cheng Fang, Liyi Shi, Hang Hu, Jianping Zhang and Dengsong Zhang*

Herein, we have rationally designed and originally fabricated a high-performance monolith catalyst based on 3D hierarchical foam-like $Fe_2O_3$@$CuO_x$ for selective catalytic reduction (SCR) of NO with $NH_3$. The $Fe_2O_3$@$CuO_x$ foam catalyst was synthesized by calcining the Cu foam in air first to form $CuO_x$ foam with $CuO_x$ nanowire arrays on the surface and then the $Fe_2O_3$ could be *in situ* formed on the surface of $CuO_x$ through the reaction in the interfacial region between the aqueous solution of $Fe^{2+}$ and CuO *via* a hydrothermal method. This catalyst was mainly characterized by the techniques of X-ray diffraction, transmission electron microscopy, scanning electron microscopy, X-ray photoelectron spectroscopy, $H_2$ temperature-programmed reduction, $NH_3$/NO + $O_2$ temperature-programmed desorption and *in situ* diffuse reflectance infrared Fourier transform spectroscopy. Both the atomic concentration of $Cu^+$ and chemisorbed oxygen species are enhanced by the coating of $Fe_2O_3$, which facilitates NO attack on active sites, resulting in the *in situ* formation of $NO_2$ and promoting the "fast SCR" reaction. Moreover, there is a strong interaction between $CuO_x$ and $Fe_2O_3$, which could not only lead to better reduction ability but also raise the acid amounts and enhance the acid strength as well as $NO_x$ adsorption ability. Based on these favourable properties, the $Fe_2O_3$@$CuO_x$ catalyst exhibits a higher activity and more extensive operating temperature window than the catalyst without $Fe_2O_3$. More importantly, the $Fe_2O_3$ not only prevents the generation of ammonium sulfates from blocking the active sites but also inhibit the formation of copper sulfates, resulting in a high $SO_2$-tolerance. In addition, the catalyst also displays favourable stability and $H_2O$ resistance. The rational design of 3D hierarchical foam-like $Fe_2O_3$@$CuO_x$ paves a new way for the development of environmental-friendly and high-performance monolith de$NO_x$ catalysts

## 1. Introduction

Nitrogen oxides ($NO_x$) from combustion of fossil fuels have given rise to a variety of environmental and health-related issues, including acid rain, photochemical smog, greenhouse effect and ozone depletion. Selective catalytic reduction (SCR) with ammonia is considered to be the most efficient and widely used technology for reducing $NO_x$ emissions from stationary source.[1-4] The commercial catalysts for this process are based on the $V_2O_5/TiO_2$ promoted by $WO_3$ or $MoO_3$. However, due to the such disadvantage as the narrow operation temperature window (300-400 $^oC$) as well as the toxicity of $VO_x$ to eco-environment and human health,[5, 6] more and more researchers are focusing on the development of environmental-friendly and vanadium-free catalysts in an appropriate temperature range.[7-11]

In the past decades, a variety of transition metal oxide based catalysts have been developed for possible application in SCR reactions.[12-15] Great efforts have been made to the $CuO_x$-based catalysts due to the good low-temperature $NH_3$-SCR activities.[16-22] However, it is well known that the residual $SO_2$ in the flue gas could greatly affects the $NO_x$ removal efficiency over $CuO_x$-based catalysts in the complicated SCR process.[22-24] Thus, it is of great significance to improve the $SO_2$-tolerance for the $CuO_x$-based catalysts.

Recently, iron oxide is widely used in the SCR of NO either as a promoter or as an active component.[25-27] It is found that the addition of Fe could improve the low-temperature SCR activity of the catalysts.[28, 29] Besides, it is also demonstrated that the $SO_2$ durability of the catalysts could be improved by the element of Fe.[25, 30, 31] Therefore, iron oxide could be a good candidate to enhance the low-temperature SCR activity and $SO_2$ tolerance for the $CuO_x$-based catalysts.

Journal Name RSCPublishing

ARTICLE

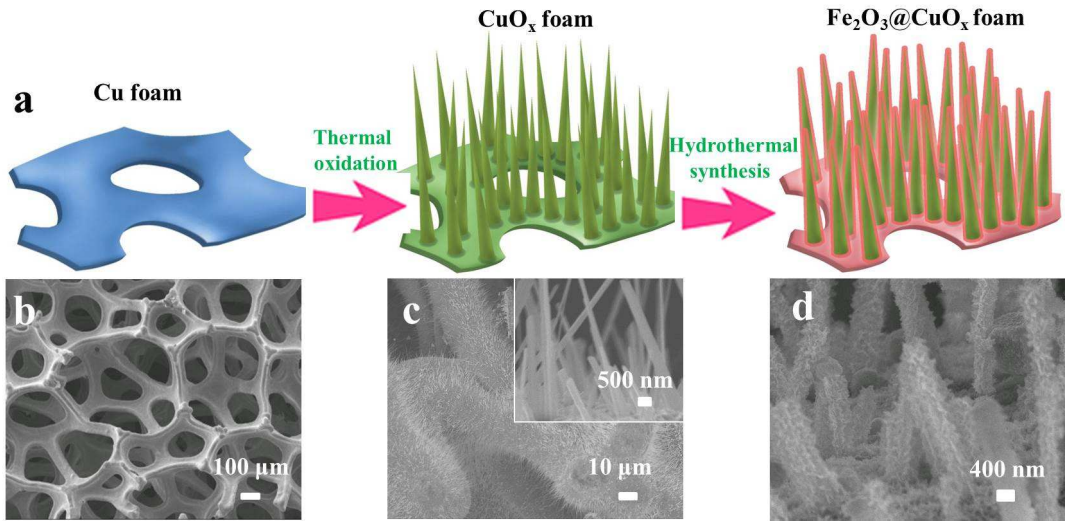


**Fig. 1.** (a) Schematic illustration of the synthetic procedure for the $Fe_2O_3$@$CuO_x$ foam. SEM images of (b) the Cu foam, (c) the $CuO_x$ foam (inset: enlarged image) and (d) the $Fe_2O_3$@$CuO_x$ foam.

It is noted that the above-mentioned catalyst powders were usually shaped as ceramic monoliths in practical applications. The catalytic components are generally introduced onto the surface of the ceramic monoliths by wash-coating or mixing into the channel walls during the extrusion of monolith structures, followed by such drawbacks as suppressed radial mixing due to impermeable internal channel walls and the accumulation of catalyst powders in the corners of the channels.[32, 33] Besides, the distribution of active components over the conventional monolith catalysts is always inhomogeneous and easy to agglomerate, which restricts the $deNO_x$ performance in the practical applications.[34, 35] Thus, it is valuable to develop high-performance monolith catalysts with stable and highly dispersed active components on the surface.

It has been reported that $Fe_2O_3$ nanosheets could be *in situ* formed on the surface of CuO through the reaction in the interfacial region between the aqueous solution of $Fe^{2+}$ and CuO.[36] Besides, the thermal oxidation of copper substrates such as grids and foils in air would cause the change of metal Cu to copper oxides and the formation of $CuO_x$ nanowires on the surface.[37] Inspired by these researches, we originally designed a three-dimensional hierarchical monolith $deNO_x$ catalyst derived from Cu foam with stable and highly dispersed active components, that is, $CuO_x$ foam with $CuO_x$ nanowire arrays on the surface coated with $Fe_2O_3$. In this design, the monolith catalysts based on the merits of copper catalysts and iron catalysts have a broaden temperature window for deNOx and also have a better catalytic performance within the low temperature regions as compared with the commercial vanadium-based catalysts. Specifically, the $CuO_x$ exhibits favorable SCR activity in low temperature region and the $Fe_2O_3$ could serves as effective components to improve the activity of $CuO_x$. Furthermore, the $Fe_2O_3$ not only prevents the generation of ammonium sulfates from blocking the active sites but also inhibit the formation of copper sulfates. The $CuO_x$ foam with a 3D interconnected porous structure possesses a high porosity and highly accessible surface area, which is beneficial to mass transfer and thus enhance the catalytic reaction.[38] As illustrated in Fig. 1a, the fabrication process of foam-like $Fe_2O_3$@$CuO_x$ monolith catalyst involves the following steps. Firstly, the $CuO_x$ foam with $CuO_x$ nanowires oriented perpendicular to the surface was formed by thermal oxidation of Cu foam in flow air. Secondly, $Fe^{2+}$ could hydrolyze and released an $H^+$ under hydrothermal conditions. Subsequently, $CuO_x$ was gradually dissolved into the aqueous solution under such local acidic environment and then the initial nucleated iron hydroxide species seeds would *in situ* form on the surface of $CuO_x$, which will serve as nucleation centers that allow the subsequent adsorption of $Fe^{2+}$ and the crystal growth. After calcination, the hierarchical foam-like $Fe_2O_3$@$CuO_x$ can be obtained. The catalyst shows uniform three-dimensional structure with homogeneous distribution of the active components and good adhesion of $Fe_2O_3$ on the foam substrate, and thus the high $NH_3$-SCR activity as well as high $SO_2$-tolerence could be guaranteed.

## 2. Experimental

### 2.1 Catalyst preparation

The Cu foam was purchased from Ailantian Advanced Technology Materials Co. Ltd (Dalian, China). The Cu foam was cut into small rounds (d = 20 mm, 1.6 mm thick) and pretreated with acetone and 0.1 M HCl aqueous solution upon ultrasonic vibration for 10 min to remove dirt and grease respectively, and then washed fully with deionized water to remove residual HCl. All the other chemicals were purchased from Sinopharm Chemical Regent Company and used without further purification.

In a typical synthesis process, the cleaned Cu foam was firstly calcined in flow air at 500 $^{o}$C for 6 h to obtain a copper oxides foam with nanowires on the surface according to previous report.[37] This sample was denoted as $CuO_x$ foam. Secondly, 1.4 mmol of $FeSO_4 \cdot 7H_2O$ was dissolved in 70 mL of water under stirring and then transferred into a Teflon-lined stainless steel autoclave. The $CuO_x$ foam was immersed in the above homogeneous solution and 2.5 mmol of sodium hydroxide was quickly added. Subsequently, the autoclave was heated and maintained at 170 $^{o}$C for 1 h and then allowed to cool down to room temperature naturally. The sample was washed several times with distilled water, dried at 80 $^{o}$C and finally calcined in air at 500 $^{o}$C for 1 h. The as-prepared catalyst was denoted as $Fe_2O_3$@$CuO_x$ foam.

### 2.2 Characterization

The powder X-ray diffraction (XRD) was performed with a Rigaku D/MAX-2200 X-ray diffractometer by using Cu Kα (40 kV, 40 mA) radiation and a secondary beam graphite monochromator. The morphologies were observed by a scanning electron microscope (SEM, JEOL JSM-6700F) and a field emission high resolution transmission electron microscope (HRTEM, JEOL JEM-2100F). The X-ray photoelectron spectroscopy (XPS) was recorded on a Perkin–Elmer PHI 5000C ESCA system equipped with a dual X-ray source, using the Mg*Kα* (1253.6 eV) anode and a hemispherical energy analyzer. The back ground pressure during data acquisition was kept below $10^{-6}$ Pa. All binding energies were calibrated using contaminant carbon (C 1s = 284.6 eV) as a reference.

Temperature-programmed reduction by hydrogen ($H_2$-TPR) was obtained on a Tianjin XQ TP5080 auto-adsorption apparatus. 50 mg of the calcined catalyst was outgassed at 300 $^{o}$C under $N_2$ flow. After cooling to room temperature under $N_2$ flow, the flowing gas was switched to 5% $H_2/N_2$, and the sample was heated to 880 $^{o}$C at a ramping rate of 10 $^{o}$C·min$^{-1}$. The $H_2$ consumption was monitored by a TCD. Temperature-programmed desorption experiments of ammonia ($NH_3$-TPD) were conducted on a Tianjin XQ TP5080 auto-adsorption apparatus. Before TPD, each sample was pretreated under $N_2$ flow at 300 $^{o}$C for 0.5 h, then saturated with high-purity anhydrous ammonia at 100 $^{o}$C for 1 h and subsequently flushed at the same temperature for 1 h. Finally, the TPD operation was carried out from 100 to 980 $^{o}$C at a heating rate of 10 $^{o}$C·min$^{-1}$. The amount of $NH_3$ desorbed was monitored by a TCD. Temperature-programmed desorption experiments of NO + $O_2$ (NO + $O_2$-TPD) were conducted on a Tianjin XQ TP5080 auto-adsorption apparatus. Before TPD, each sample was pretreated under He flow at 300 $^{o}$C for 0.5 h, then the adsorption was performed by passing a mixed gas containing 500 ppm NO + 5 % $O_2$ with He as the balance at room temperature for 1 h and subsequently flushed for another 1 h. Finally, the TPD operation was carried out from 30 to 480 $^{o}$C at a heating rate of 10 $^{o}$C·min$^{-1}$. The amount of $NO_x$ desorbed was monitored by a TCD.

*In situ* diffuse reflectance infrared Fourier transform spectroscopy (*in situ* DRIFTS) experiments were performed on an FTIR spectrometer (Nicolet 6700) equipped with a Harrick DRIFT cell and an MCT/A detector cooled by liquid $N_2$. Prior to each experiment, the catalysts were pretreated at 500 $^{o}$C in a flow of $N_2$ (50 mL·min$^{-1}$) for 0.5 h and cooled to room temperature under $N_2$ flow. Background spectra were recorded in the $N_2$ flow at different temperature and subtracted from each sample spectrum. All the *in situ* DRIFTS spectra were collected by accumulating 64 scans at a 4 cm$^{-1}$ resolution. For ammonia adsorption, the catalysts were treated in flow of 500 ppm $NH_3$ at room temperature for 1 h and then purged by $N_2$.

### 2.3 Catalytic activity measurements

The $NH_3$-SCR activity measurement was carried out in a fixed-bed stainless steel flow reactor (i.d. 2 cm) operating in a steady state flow mode. The reactant gases were fed to the reactor by an electronic mass flow controller. The typical reactant gas composition was as follows: 500 ppm NO, 500 ppm $NH_3$, 3 vol. % $O_2$, 250 ppm $SO_2$ (when used), 8 vol. % $H_2O$ (when used), and balance $N_2$. The total flow rate was 215 mL·min$^{-1}$ and thus a GHSV of 20 000 h$^{-1}$ was obtained. The temperature increased from 200 to 400 $^{o}$C. At each temperature step the data were recorded when the SCR reaction reached steady state after 15min. The concentration of NO in the inlet and outlet gas was measured by a KM9106 flue gas analyzer. NO conversion was calculated according to the following expression:

$$\text{NO Conversion}(\%) = \frac{[NO]_{in} - [NO]_{out}}{[NO]_{in}} \times 100\% \qquad (1)$$

## 3. Results and discussion

### 3.1. Characteristics

The micro-morphologies of the catalysts were investigated by SEM techniques. Fig. 1b shows that the framework of Cu foam forms a three-dimensional interconnected microporous structure. The surface of Cu foam shows a tortoiseshell-like morphology and many tiny pores. The Cu foam possesses a high porosity and highly accessible surface area, which is conducive to mass transfer. After thermal oxidation in flow air, the surface of the framework is covered by a dense array of uniform, straight and long nanowires as shown in Fig. 1c. The inset of Fig. 1c reveals that the surface of the nanowires is smooth and round. The diameter of these nanowires is about 500 nm and the length is varied in the range of 2-10 μm.[37] Each

nanowire is grown in the direction perpendicular to the framework. Fig. 1d shows the SEM image of the $Fe_2O_3$@$CuO_x$ foam. It is obvious that the surface of the nanowires is rough and some irregular nanoparticles distributed around the nanowire. The shape and size of the nanowire did not significantly change from that of $CuO_x$ foam as presented in the inset of Fig. 1c.

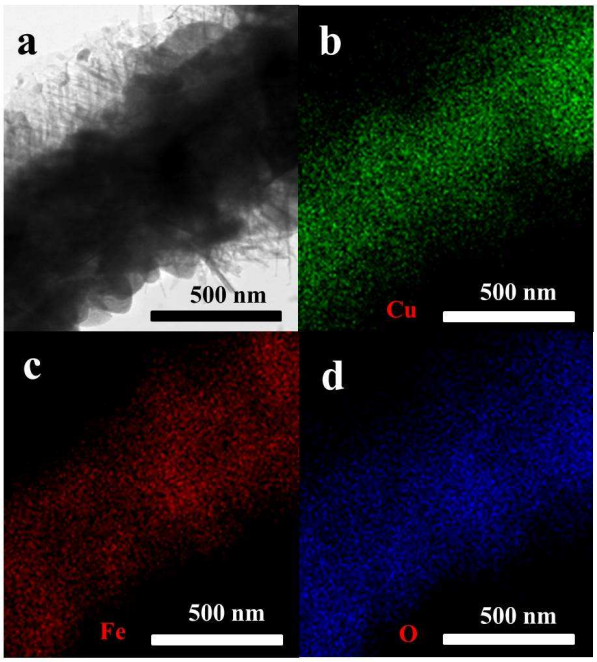


**Fig. 2.** TEM image (a) and EDX-mapping images (b-d) of the $Fe_2O_3$@$CuO_x$ foam.

The TEM analysis was also performed to investigate morphological characteristics of the $Fe_2O_3$@$CuO_x$ foam as shown in Fig. 2. Fig. 2a clearly exhibits that the nanowire is wrapped by nanoparticles. As compared to the inset of Fig. 1c, the only difference is that the smooth nanowire surface of $CuO_x$ foam disappeared and irregular nanoparticles were uniformly scattered on the surface instead. Fig. 2b-d are the distributions of Cu, Fe, and O elements on the surface of the $Fe_2O_3$@$CuO_x$ foam, which can be verified by the EDX mapping from the TEM image in Fig. 2a. The mapping shapes of Cu, Fe, and O elements are all similar to that of the $Fe_2O_3$@$CuO_x$ foam, indicating the catalyst has uniform element composition and dispersion. It also presents that the presence of Cu is associated with Fe, which suggests the synergistic effect between Cu and Fe species.

The XRD was performed to determine the chemical compositions and phases of all catalysts as shown in Fig. 3. As to the Cu foam, the diffraction peaks are corresponding to the typical and sole elemental Cu (JCPDS 65-9026), suggesting the high purity of the Cu foam. For the $CuO_x$ foam, the peaks belonging to the phase of metal Cu disappear completely. Specifically, the strong diffraction peaks at around 35.5 °, 38.7 °, 48.7 ° and 61.5 ° can be assigned to the CuO (JCPDS 48-1548) and the diffraction peaks around 36.5 °, 42.4 ° and 73.7 ° according to $Cu_2O$ (JCPDS 65-3288) can be observed. These results indicate the fully oxidation of the Cu foam, which is in line with the previous study.[37] It is reported that $Cu_2O$ was first generated when copper was oxidized in air and then it served as a precursor to CuO, which was formed slowly through a second step of oxidation.[37] The XRD pattern of $Fe_2O_3$@$CuO_x$ foam is very similar to that of $CuO_x$ foam but there are two extra weak peaks corresponding to $Fe_2O_3$ (JCPDS 39-1346). The peaks of $Fe_2O_3$ shows that iron species generated on the $CuO_x$ foam during the hydrothermal treatment, coinciding with the SEM and TEM results. In addition, a slight shift of the XRD peaks can be found, which should be ascribed to the interaction between $Fe_2O_3$ and $CuO_x$.

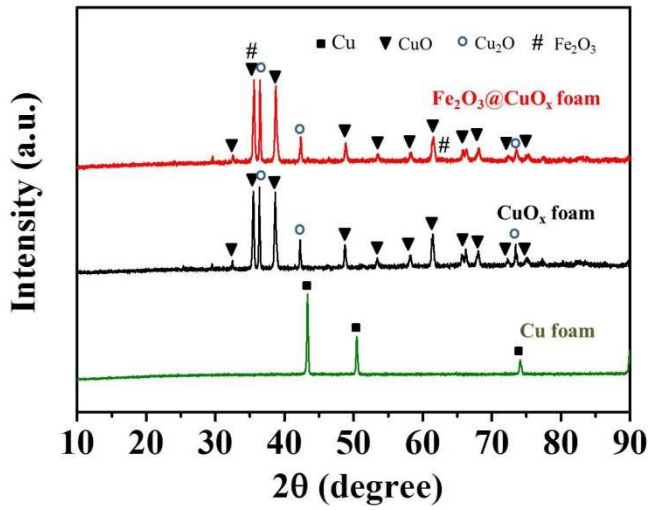


**Fig. 3.** XRD patterns of the catalysts.

The XPS measurements were carried out to determine the oxidation state of elements as well as the chemical compositions of the catalysts. The Cu 2p spectra of $Fe_2O_3$@$CuO_x$ foam and $CuO_x$ foam can be observed in Fig. 4a, which can be separated into four peaks by performing a peak-fitting deconvolution.[22, 39] The spectra located at 930-937 eV can be separated into two peaks assigned to $Cu^+$ (932.4 eV) and $Cu^{2+}$ (934.3 eV). The shake-up satellite peaks at 940-945 eV can also be observed, which is attributed to the characteristics of $Cu^{2+}$. The surface atomic concentrations of O, Cu, Fe and the relative concentration ratios of $Cu^+$ and surface adsorbed oxygen are summarized in Table 1. The relative intensity of $Cu^+/Cu^{2+}$ calculated from deconvolution of Cu 2p profiles were 0.7 and 0.6 for the $Fe_2O_3$@$CuO_x$ foam and $CuO_x$ foam, respectively. This result means that the introduction of $Fe_2O_3$ will improve the content of $Cu^+$. It has been reported that $Cu^+$ was suggested to facilitate NO attack on active sites, resulting in the *in situ* formation of $NO_2$, which might promote the "fast SCR" reaction as the presence of $NO_2$ in the feed gas is conducive to the SCR reaction over the catalysts.[24, 40] Compared with the $CuO_x$ foam, the Cu 2p peaks for the $Fe_2O_3$@$CuO_x$ foam catalyst show a little positive shift in binding energy due to the electron transfer from Cu to Fe.[41] Therefore, Cu species have lower density of electron cloud,

Journal Name RSCPublishing

ARTICLE

**Table 1** Elemental surface analysis of the catalysts by XPS.

| Catalyst | O (at.%) | Cu (at.%) | Fe (at.%) | $Cu^+$ (at.%) | $O_\alpha/(O_\alpha+O_\beta)$ (%) | $O_\alpha$ (at.%) |
|---|---|---|---|---|---|---|
| $Fe_2O_3$@$CuO_x$ foam | 38.7 | 5.3 | 0.8 | 2.2 | 62.8 | 24.3 |
| $CuO_x$ foam | 39.1 | 3.9 | - | 1.5 | 59.1 | 23.1 |

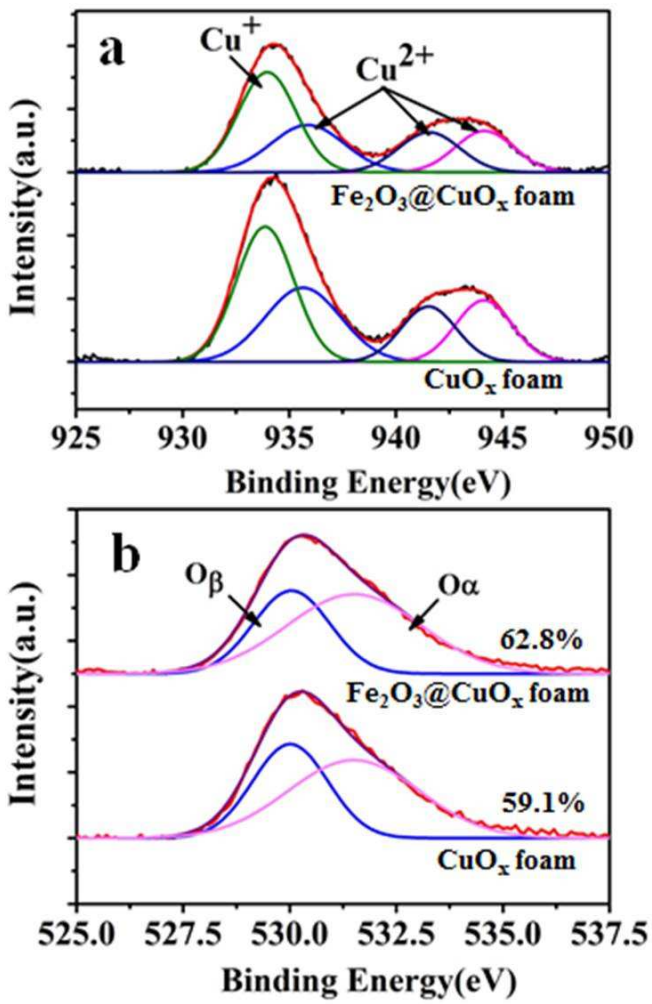


**Fig. 4.** XPS spectra for (a) Cu 2p and (b) O 1s of the catalysts.

leading to increase of the oxidative ability of Cu species in the $Fe_2O_3$@$CuO_x$ foam.[41] In other words, this positive shift suggests the change in the chemical environment of Cu, indicating there is an interaction between Cu and Fe species. In the Fe 2p XPS spectra of the $Fe_2O_3$@$CuO_x$ foam (Fig. S1, ESI), the binding energies of the three peaks correspond well with characteristic $Fe^{3+}$, suggesting the presence of $Fe_2O_3$.[41-43]

In the case of O 1s spectra (Fig. 4b), the spectra of the catalysts can be divided into two peaks. The peak at lower binding energy (528.7-530.9 eV) is assigned to the lattice oxygen $O^{2-}$ (denoted as $O_\beta$), and the one at higher binding energy (531.4-532.5 eV) corresponds to the surface adsorbed oxygen (denoted as $O_\alpha$), belonging to hydroxyl-like or defect-oxide group.[44] The $O_\alpha/(O_\alpha+O_\beta)$ over the $Fe_2O_3$@$CuO_x$ foam and $CuO_x$ foam are presented as 62.8 % and 59.1 % and the concentration of $O_\alpha$ are calculated to be 24.3 at.% and 23.1 at.%, respectively. It has been demonstrated that the surface adsorbed oxygen $O_\alpha$ is more active in oxidation reactions than the lattice oxygen $O_\beta$ due to its higher mobility. It is believed that high $O_\alpha$ content promotes NO oxidation to $NO_2$, thereafter facilitates the "fast SCR" reaction.[45] Furthermore, the surface hydroxyl-like groups could act as Brønsted acid sites to absorb $NH_3$ and form $NH_4^+$, which will react with the $NO_2$ adsorbed nearby to produce $N_2$.[46] Based on the XPS analysis, higher $O_\alpha$ concentration over the $Fe_2O_3$@$CuO_x$ foam would lead to favorable reduction of NO through the "fast SCR" reaction.

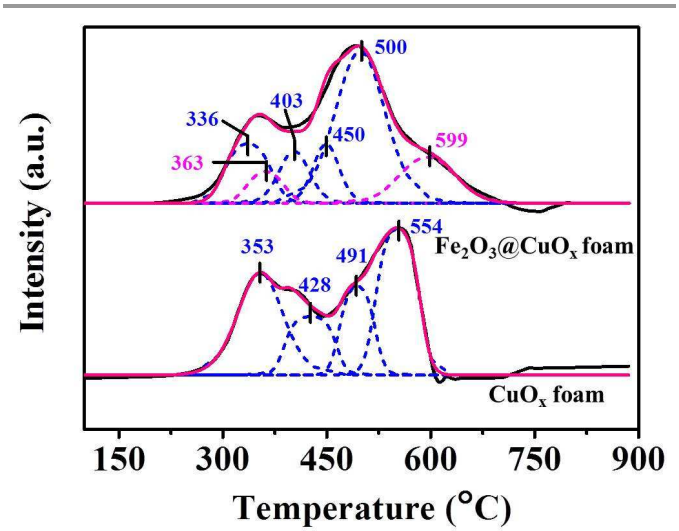


**Fig. 5.** $H_2$-TPR profiles of the catalysts.

The $H_2$-TPR technique was employed to investigate the reducibility of the catalysts. As illustrated in Fig. 5, all the $H_2$-TPR profiles of the $Fe_2O_3$@$CuO_x$ foam and $CuO_x$ foam present distinct $H_2$ consumption peaks. It has also been reported that CuO are more easily reduced than other $CuO_x$ with different oxidation states and the profile of pure CuO exhibits reduction peak at approximately 370 °C.[47, 48] For the $CuO_x$ foam, the $H_2$-TPR profile presents two well-defined reduction peaks around 353 and 554 °C. The former can be assigned to the relatively easier reduction in the $CuO_x$ dispersed on the outside surface of the catalyst, while the latter took place inside the bulk catalyst. In order to clarify the detailed reduction processes, the reduction peaks were deconvoluted into four sub-bands from low to high temperature, attributed to the reduction processes of CuO → $Cu_2O$ and $Cu_2O$ → Cu in the surface and bulk, respectively. It has been demonstrated that the $H_2$-TPR profile of $Fe_2O_3$ presents two $H_2$ consumption peaks around 370 and 590 °C, ascribed to the stepwise reduction of $Fe^{3+}$ → $Fe^{2+}$ → $Fe^0$.[41] The reduction peaks of the $Fe_2O_3$@$CuO_x$ foam were accordingly deconvoluted into six sub-bands. The four peaks at 336 °C, 403 °C, 450 °C and 500 °C are attributed to the reduction of $CuO_x$ and the two peaks at 363 °C and 599 °C corresponds to the reduction of $Fe_2O_3$. The reduction peaks of $CuO_x$ species for $Fe_2O_3$@$CuO_x$ foam shift to the low-temperature regions by about 20-50 °C as compared to the $CuO_x$ foam, suggesting the better redox ability. Thus, it is reasonable to deduce that the introduction of $Fe_2O_3$ promotes the reducibility of $CuO_x$ and there is a strong interaction between copper oxide and iron oxide species in the $Fe_2O_3$@$CuO_x$ foam, which was also confirmed by the Cu 2p XPS results. Moreover, the area of the reduction peak is actively relevant with the consumption of $H_2$, directly revealing the amount of the reactive oxygen species.[49] Larger reduction peaks can be observed for the $Fe_2O_3$@$CuO_x$ foam, suggesting that more active components are exposed, which is conducive to the SCR reaction.

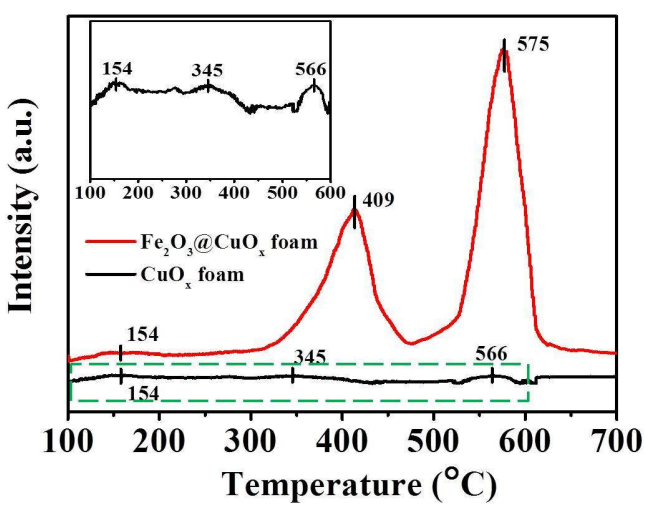


**Fig. 6.** $NH_3$-TPD profiles of the catalysts (the inset is the enlargement of the $CuO_x$ foam).

The $NH_3$-TPD analyses were performed to study the adsorption behaviour of $NH_3$ on the catalysts, which is generally viewed as the primary steps in the $NH_3$-SCR of NO. It is reported that for the $NH_3$-TPD profiles, the low temperature desorption peaks between 100 and 300 °C belong to the ammonia desorbed from weak Lewis or Brønsted acid sites, whereas, the high temperature desorption peaks situated between 300 and 600 °C belong to the ammonia desorbed from strong acid sites.[50] As shown in Fig. 6, the $NH_3$-TPD profile of $Fe_2O_3$@$CuO_x$ foam exhibits three desorption peaks: the weak peak centered at 154 °C attributed to ammonia desorbed from the weak acid sites, and the two strong and sharp peaks observed at 409 and 575 °C assigned to ammonia desorbed from the strong acid sites on the catalysts. While, in the case of $CuO_x$ foam, the intensity of the desorption peaks is significantly reduced. In the inset of Fig. 6, the enlarged profile of $CuO_x$ foam also shows three desorption peaks. The peak centered at 154 °C and the other two peaks at 345 and 566 °C are related to the weak and strong acid sites, respectively. It is well known that the position and area of desorption peak are correlated with the acid strength and acid amount, respectively.[9, 51] The peaks related to strong acid sites of the $CuO_x$ foam shift to higher temperatures after the coating of $Fe_2O_3$, which suggests that the strength of the acid sites on the $Fe_2O_3$@$CuO_x$ foam is stronger than that of the $CuO_x$ foam. Therefore, the stronger acid strength of the $Fe_2O_3$@$CuO_x$ foam might be associated with the stronger interaction between copper oxide and iron oxide. It is also demonstrated that $Fe^{3+}$ could act as strong Lewis acid sites.[43] The $NH_3$-TPD profile of the $Fe_2O_3$@$CuO_x$ foam reveals the much larger area, indicating the presence of more acid sites. The above results demonstrate that the coated $Fe_2O_3$ not only enhance the acid strength but also raise acid amounts, which may be beneficial to the $NH_3$-SCR reaction.

The *in situ* DRIFTS of $NH_3$ adsorption at various temperatures are also performed to investigate the adsorption behaviours of the $NH_3$ molecules on the surface of the catalysts. As shown in Fig. 7, the bands at 1247 and 1618 $cm^{-1}$ can be assigned to the characteristic bands of $NH_3$ coordinated on Lewis acid sites. As compared with the $CuO_x$ foam, the band at 1618 $cm^{-1}$ shows up for the $Fe_2O_3$@$CuO_x$ foam, which can be assigned to the formation of new Lewis acid site caused by the addition of $Fe_2O_3$. No bands assigned to Brønsted acid sites were observed, indicating that Lewis acid sites are responsible for the SCR reactions over these two catalysts. It is evident that the band intensity of Lewis acid over the $Fe_2O_3$@$CuO_x$ foam is much higher than that over the $CuO_x$ foam. This result suggests the addition of $Fe_2O_3$ will lead to more Lewis acid sites due to the interaction between $CuO_x$ and $Fe_2O_3$, and thus result in more adsorbed $NH_3$, which is in good agreement with the $NH_3$-TPD analysis. A shift of the band at 1247 $cm^{-1}$ both occurs in the *in situ* DRIFTS process for the two catalysts, which can be attributed to electron donation from (partly) filled *d*-orbitals of copper ions to $\pi^*$-orbitals of $NH_3$.[52] It is also found that when the temperature goes up to 100 °C over the $Fe_2O_3$@$CuO_x$ foam, the intensity of band at 1247 $cm^{-1}$ increases. This phenomenon can be attributed to the activation of $NH_3$ molecules caused by

heating up and subsequently $NH_3$ molecules are adsorbed by Lewis acid sites from the gaseous phase. The above analyses indicate the coating of $Fe_2O_3$ on the $CuO_x$ foam has enhanced the Lewis acid sites over the $CuO_x$ foam, resulting in the better low-temperature $NH_3$-SCR activity.

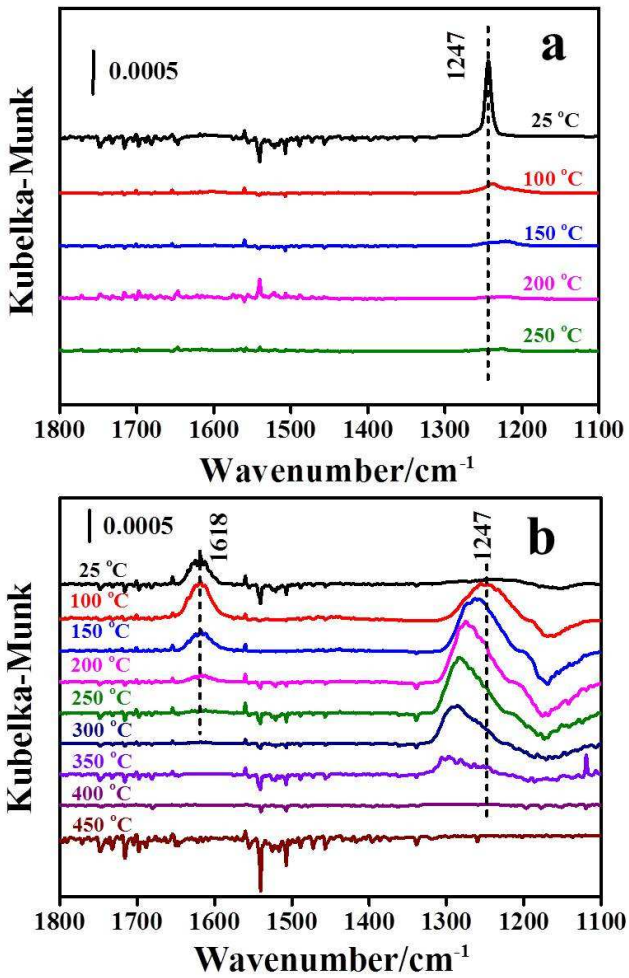


**Fig. 7.** *In situ* DRIFTS of $NH_3$ adsorption on (a) the $CuO_x$ foam and (b) the $Fe_2O_3$@$CuO_x$ foam.

The NO + $O_2$-TPD measurements were also conducted to study the adsorption behaviour of $NO_x$ on the catalysts as presented in Fig. 8. The TPD profiles of the two catalysts both exhibit distinct $NO_x$ desorption peaks. It is reported that the $NO_x$ desorption process can be divided into three stages: simple desorption of physical adsorbed and weakly chemisorbed NO (75-150 °C), NO desorption together with its dissociation (150-400 °C), and nitrite/nitrate thermal decomposition (300-500 °C).[53] Accordingly, in the case of the $Fe_2O_3$@$CuO_x$ foam and the $CuO_x$ foam, the desorption peaks at 77 °C correspond to the physical adsorbed NO, and the ones at 170 °C, 198 °C and 228 °C are assigned to the desorption and dissociation of NO, and the ones at 378 °C and 430 °C are attributed to the thermal decomposition of nitrite/nitrate species. As compared with the $CuO_x$ foam, the desorption peaks shift to higher temperature range after the introduction of $Fe_2O_3$ and the NO + $O_2$-TPD profile of $Fe_2O_3$@$CuO_x$ foam reveals the much larger area, suggesting the interaction between iron oxide and copper oxide species can lead to the stronger adsorption ability of $NO_x$ and more adsorbed $NO_x$ over the catalyst, which are both beneficial to the de$NO_x$ process.

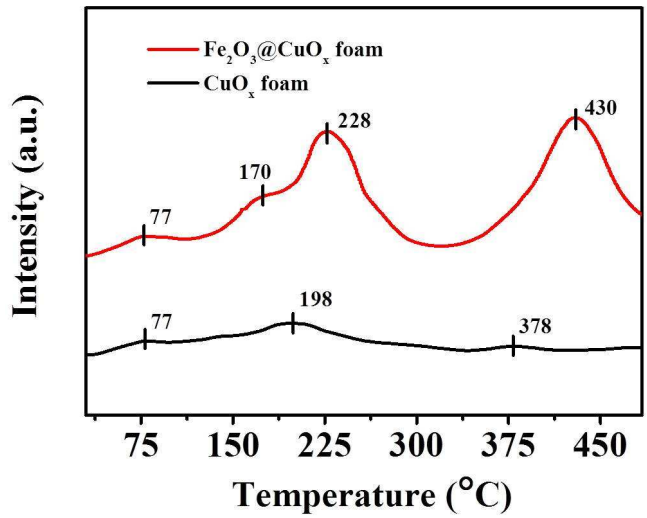


**Fig. 8.** NO + $O_2$-TPD profiles of the catalysts.

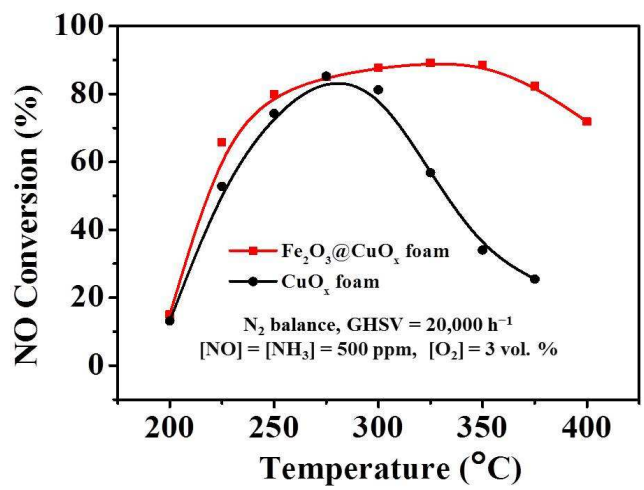


**Fig. 9.** Plots of NO conversion of the catalysts *vs.* temperature.

### 3.2. Catalytic activity

The $NH_3$-SCR activities tested for the catalysts as a function of temperature is provided in Fig. 9. It is clear that the $Fe_2O_3$@$CuO_x$ foam demonstrates a more extensive operating temperature window and higher NO conversion than the $CuO_x$ foam under identical operating conditions. For the $CuO_x$ foam catalyst, the maximum NO conversion is 83% at 275 °C, and the NO conversion is dramatically decreased when the operating temperature is beyond 300 °C. After coating with $Fe_2O_3$, by contrast, the maximum NO conversion is enhanced to 90% and the temperature window is significantly broadened, especially at the high temperature region. The temperature window for >80% NO conversion ranges from 250 to 380 °C.

Journal Name RSCPublishing

ARTICLE

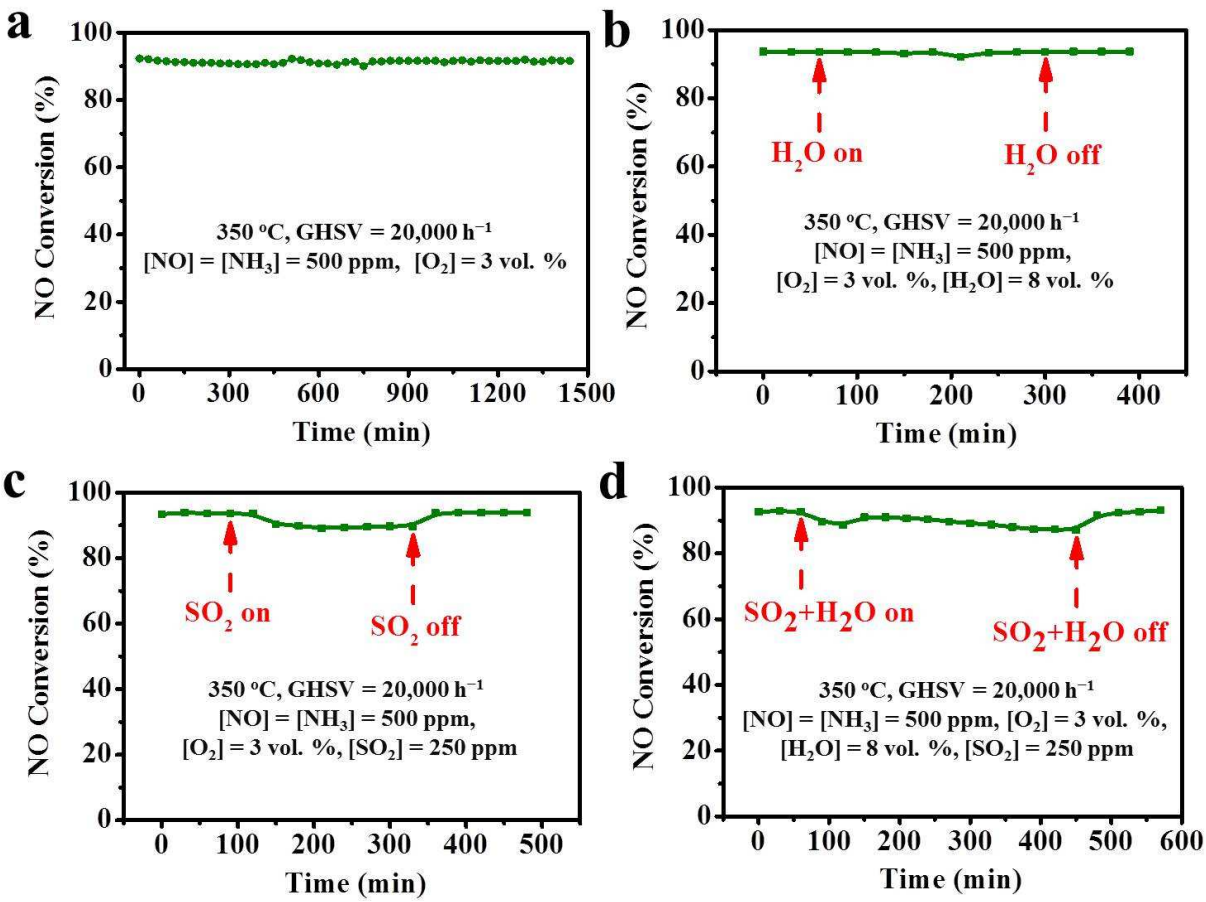


**Fig. 10.** $NH_3$-SCR performance of the $Fe_2O_3$@$CuO_x$ foam.

Based on these results, the $Fe_2O_3$ could serve as effective components to promote the catalytic activity of the catalyst, especially at the high-temperature region. Besides, the $Fe_2O_3$@$CuO_x$ foam achieves higher $N_2$ selectivity than the $CuO_x$ foam under the operating conditions (Fig. S2, ESI). The catalytic activity curve of Cu foam is similar to that of $CuO_x$ foam (Fig. S3, ESI), which can be attributed to the copper oxide species formed during the temperature-rising test process.

The XRD, SEM, TEM and EDX-mapping analyses demonstrate the successful coating of $Fe_2O_3$ on the $CuO_x$ foam and the uniform distribution of active components, which could greatly improve the catalytic activity of the catalysts.[54] According to the XPS analyses, the introduction of $Fe_2O_3$ could increase the amount of $Cu^+$ and surface adsorbed oxygen species on the surface of catalyst. In addition, a large amount of $Cu^+$ (1.6 at.%) still exists on the surface of the used $Fe_2O_3$@$CuO_x$ foam (Fig. S4, ESI). The XRD result of the used $Fe_2O_3$@$CuO_x$ foam also confirms the presence of $Cu_2O$ (Fig. S5, ESI). The $H_2$-TPR analyses suggest that the $Fe_2O_3$@$CuO_x$ foam possess abundant reactive oxygen species and strong interaction between $CuO_x$ and $Fe_2O_3$, resulting in its better reducibility, which could enhance the catalytic cycle. The $NH_3$-TPD and *in situ* DRIFTS results show that the $Fe_2O_3$@$CuO_x$ foam presents more acid sites and stronger acid strength, which could facilitate the adsorption and activation of $NH_3$ in the SCR reaction. Stronger adsorption ability of $NO_x$ and more adsorbed $NO_x$ over the $Fe_2O_3$@$CuO_x$ foam are also proved by the NO + $O_2$-TPD tests. In addition, the 3D hierarchical structure can improve the gas diffusion by providing a decreased gas diffusion distance and also ensuring a minimized inner resistance for the gas transportation pathways. Based on these favorable properties of the structure and components, the $Fe_2O_3$@$CuO_x$ foam catalyst exhibits excellent activity in the $NH_3$-SCR reaction.

The stability is also an important indicator to evaluate the catalytic performance of the catalyst. Fig. 10a shows the

stability test of the $Fe_2O_3$@$CuO_x$ foam as a function of time at 350 °C. The feed gas consists of 500 ppm NO, 500 ppm $NH_3$, 3 vol% $O_2$, and balance gas $N_2$ and the total flow rate is 215 mL $min^{-1}$. The NO conversion of the catalyst is kept at ca. 91.5% during a 24 h continuous running duration. Therefore, the $Fe_2O_3$@$CuO_x$ foam catalyst could not only provide high $NH_3$-SCR activity in a wide operating temperature range, but also exhibit good stability.

It is noted that vapour in the flue gas might have an inhibition effect on the $NO_x$ removal capacity of catalysts.[26, 55] The influence of $H_2O$ on the SCR activity over the $Fe_2O_3$@$CuO_x$ foam as a function of time at 350 °C is investigated as shown in Fig. 10b. Before the addition of vapour, the NO conversion of the catalyst is kept at ca. 92%. When 8 vol. % $H_2O$ is added to the feed gas, the NO conversion is almost unchanged with a slight fluctuation during the test period. This result indicates that the catalyst has a good $H_2O$-resistant performance. It has also been reported that the inhibition of $H_2O$ is reversible, due to the competitive adsorption between water and ammonia molecules on the active sites of the catalyst surface.[55] The $NH_3$-TPD analysis shows that a large number of acid sites over the $Fe_2O_3$@$CuO_x$ foam might preferentially absorb $NH_3$ other than $H_2O$ in the gas phase, which is responsible for its excellent $H_2O$ resistance.

As we know, the flue gas still comprises low concentration of $SO_2$ even after desulphurization.[23] It is generally believed that $SO_2$ has a serious poisoning effect on the catalytic activity and could lead to the catalysts poisoning and deactivation.[19, 56, 57] Fig. 10c depicts the catalytic activity of the catalyst, as a function of time in the presence of 250 ppm $SO_2$ at 350 °C. When 250 ppm $SO_2$ was added to the feed gases, the NO conversion over the catalyst decrease slightly, and only about 3 % of the conversion was lost during the test period. After eliminating $SO_2$ from the feed gas, the NO conversion was gradually restored to the initial value. It is noted that the poisoning and deactivation of the catalyst caused by $SO_2$ usually involves the following two aspects.[58, 59] Firstly, ammonium sulfate species are generated and deposited on the catalyst surface, blocking the active sites of the catalyst surface, and this deactivation process is reversible. Secondly, active components of the catalyst can be sulfated to form stable metal sulfates, which leads to an irreversible deactivation. Shen *et al.*[60] reported that the addition of iron oxide would have a positive effect on the $SO_2$-tolerance of Mn-Ce/$TiO_2$ catalyst, because iron oxide could significantly decrease the generation rate of sulfates. Fig. 9c indicates that the effective resistance to $SO_2$ appears to be achieved by coating $Fe_2O_3$ on $CuO_x$. Therefore, it is reasonable to deduce that the $Fe_2O_3$ not only prevent the generation of ammonium sulfates from blocking the active sites but also inhibit the formation of copper sulfates.

We also investigated the SCR activity of the $Fe_2O_3$@$CuO_x$ foam under the coexistence of $H_2O$ and $SO_2$, and the result is shown in Fig. 10d. It is obvious that the coexistence of 8 vol. % $H_2O$ and 250 ppm $SO_2$ induced a 4 % decrease in the NO conversion, but the NO conversion is recovered to 92 % when cutting off the supply of $H_2O$ and $SO_2$. The above results suggested that the synergistic inhibition effect between $H_2O$ and $SO_2$ does not exist in the SCR reaction over the catalyst. The morphology and structure of the catalyst are maintained well after the anti-toxicity test (Fig. S6, ESI). Thus, it is reasonable to deduce that the adhesion between the $Fe_2O_3$ and $CuO_x$ foam is sufficiently strong to support the de-$NO_x$ process. Besides, the XRD pattern of this catalyst shows that no crystalline phase ascribed to sulfates can be detected (Fig. S7, ESI). The maintained morphology and XRD result prove directly that the generation of ammonium sulfates and copper sulfates on the catalyst surface can be inhibited by the $Fe_2O_3$.

## 4. Conclusions

In summary, we have rationally designed and originally fabricated a monolith de$NO_x$ catalyst based on 3D hierarchical foam-like $Fe_2O_3$@$CuO_x$. The $Fe_2O_3$@$CuO_x$ foam displays a more extensive operating temperature window and higher catalytic activity for $NH_3$-SCR of NO than the $CuO_x$ foam. The characteristic of 3D hierarchical structure, uniform distribution of the active components as well as the strong interaction between copper oxide and iron oxide species contribute to the excellent de$NO_x$ performance of the $Fe_2O_3$@$CuO_x$ foam. The coating of $Fe_2O_3$ could improve the atomic concentration of the $Cu^+$ and surface adsorbed oxygen species, facilitating NO attack on active sites as well as *in situ* formation of $NO_2$. The strong interaction between copper oxide and iron oxide species lead to better reduction ability, more acid sites, stronger acid strength and $NO_x$ adsorption ability. The above features are closely associated with the excellent activity of the catalyst in the $NH_3$-SCR reaction. The catalyst also presented favourable stability and $H_2O$/$SO_2$ resistance. Especially, the $SO_2$-resistance of the $Fe_2O_3$@$CuO_x$ foam is significantly improved since the $Fe_2O_3$ not only prevents the generation of ammonium sulfates from blocking the active sites but also inhibit the formation of copper sulfates. The rational design of 3D hierarchical foam-like $Fe_2O_3$@$CuO_x$ offers fresh approach to developing eco-friendly and high-performance monolith de$NO_x$ catalysts.

## Acknowledgments

The authors acknowledge the support of the National Basic Research Program of China (973 Program, 2014CB660803), the National Natural Science Foundation of China (U1462110), the Science and Technology Commission of Shanghai Municipality (13NM1401200), and the Shanghai Municipal Education Commission (14ZZ097). We thank Mr. Y. L. Chu from the Analysis and Test Center of SHU for help with the TEM and SEM measurements.

## Notes and references

*Research Center of Nano Science and Technology, School of Material Science and Engineering, Shanghai University, Shanghai 200444, China. Fax: 86 21 66136081; E-mail: dszhang@shu.edu.cn*

Electronic Supplementary Information (ESI) available: [XPS spectra, $N_2$ selectivity, catalytic performance, XRD and SEM images of the catalysts]. See DOI: 10.1039/b000000x/


1. P. Forzatti, I. Nova and E. Tronconi, *Angew. Chem.*, 2009, **121**, 8516-8518.
2. F. Gao, E. D. Walter, N. M. Washton, J. Szanyi and C. H. F. Peden, *ACS Catal.*, 2013, **3**, 2083-2093.
3. W. C. Wang, G. McCool, N. Kapur, G. Yuan, B. Shan, M. Nguyen, U. M. Graham, B. H. Davis, G. Jacobs, K. Cho and X. Hao, *Science*, 2012, **337**, 832-835.
4. F. Thibault-Starzyk, E. Seguin, S. Thomas, M. Daturi, H. Arnolds and D. A. King, *Science*, 2009, **324**, 1048-1051.
5. R. H. Gao, D. S. Zhang, X. G. Liu, L. Y. Shi, P. Maitarad, H. R. Li, J. P. Zhang and W. G. Cao, *Catal. Sci. Technol.*, 2013, **3**, 191-199.
6. S. B. Kristensen, A. J. Kunov-Kruse, A. Riisager, S. B. Rasmussen and R. Fehrmann, *J. Catal.*, 2011, **284**, 60-67.
7. R. Nedyalkova, K. Kamasamudram, N. W. Currier, J. H. Li, A. Yezerets and L. Olsson, *J. Catal.*, 2013, **299**, 101-108.
8. S. X. Cai, D. S. Zhang, L. Zhang, L. Huang, H. R. Li, R. H. Gao, L. Y. Shi and J. P. Zhang, *Catal. Sci. Technol.*, 2014, **4**, 93-101.
9. L. Zhang, D. S. Zhang, J. P. Zhang, S. X. Cai, C. Fang, L. Huang, H. R. Li, R. H. Gao and L. Y. Shi, *Nanoscale*, 2013, **5**, 9821-9829.
10. R. H. Gao, D. S. Zhang, P. Maitarad, L. Y. Shi, T. Rungrotmongkol, H. R. Li, J. P. Zhang and W. G. Cao, *J. Phys. Chem. C*, 2013, **117**, 10502-10511.
11. L. Zhang, L. Y. Shi, L. Huang, J. P. Zhang, R. H. Gao and D. S. Zhang, *ACS Catal.*, 2014, **4**, 1753-1763.
12. C. Fang, D. S. Zhang, S. X. Cai, L. Zhang, L. Huang, H. R. Li, P. Maitarad, L. Y. Shi, R. H. Gao and J. P. Zhang, *Nanoscale*, 2013, **5**, 9199-9207.
13. J. Liu, X. Y. Li, Q. D. Zhao, C. Hao and D. K. Zhang, *Environ. Sci. Technol.*, 2013, **47**, 4528-4535.
14. H. Chang, M. T. Jong, C. Wang, R. Qu, Y. Du, J. Li and J. Hao, *Environ. Sci. Technol.*, 2013, **47**, 11692-11699.
15. F. Can, S. Berland, S. Royer, X. Courtois and D. Duprez, *ACS Catal.*, 2013, **3**, 1120-1132.
16. D. A. Pena, B. S. Uphade and P. G. Smirniotis, *J. Catal.*, 2004, **221**, 421-431.
17. G. Ramis, L. Yi, G. Busca, M. Turco, E. Kotur and R. J. Willey, *J. Catal.*, 1995, **157**, 523-535.
18. L. Chmielarz, P. Kustrowski, M. Zbroja, B. Gil-Knap, J. Datka and R. Dziembaj, *Appl. Catal., B*, 2004, **53**, 47-61.
19. J. H. Huang, Z. Q. Tong, Y. Huang and J. F. Zhang, *Appl. Catal., B*, 2008, **78**, 309-314.
20. N. Apostolescu, B. Geiger, K. Hizbullah, M. T. Jan, S. Kureti, D. Reichert, F. Schott and W. Weisweiler, *Appl. Catal., B*, 2006, **62**, 104-114.
21. H. Teng, L. Y. Hsu and Y. C. Lai, *Environ. Sci. Technol.*, 2001, **35**, 2369-2374.
22. Q. Li, H. S. Yang, Z. X. Ma and X. B. Zhang, *Catal. Commun.*, 2012, **17**, 8-12.
23. Y. S. Cheng, C. Lambert, D. H. Kim, J. H. Kwak, S. J. Cho and C. H. F. Peden, *Catal. Today*, 2010, **151**, 266-270.
24. Z. X. Ma, H. S. Yang, B. Li, F. Liu and X. B. Zhang, *Ind. Eng. Chem. Res.*, 2013, **52**, 3708-3713.
25. Y. Shu, T. Aikebaier, X. Quan, S. Chen and H. T. Yu, *Appl. Catal., B*, 2014, **150–151**, 630-635.
26. X. L. Mou, B. S. Zhang, Y. Li, L. D. Yao, X. J. Wei, D. S. Su and W. J. Shen, *Angew. Chem., Int. Ed.*, 2012, **51**, 2989-2993.
27. X. Y. Shi, F. D. Liu, L. J. Xie, W. P. Shan and H. He, *Environ. Sci. Technol.*, 2013, **47**, 3293-3298.
28. G. S. Qi and R. T. Yang, *Appl. Catal., B*, 2003, **44**, 217-225.
29. Z. B. Wu, B. Q. Jiang and Y. Liu, *Appl. Catal., B*, 2008, **79**, 347-355.
30. Y. Shu, H. Sun, X. Quan and S. Chen, *J. Phys. Chem. C*, 25319-25327.
31. S. J. Yang, J. H. Li, C. Z. Wang, J. H. Chen, L. Ma, H. Z. Chang, L. Chen, Y. peng and N. Q. Yan, *Appl. Catal., B*, 2012, **117-118**, 73-80.
32. Z. G. Lei, C. P. Wen, J. Zhang and B. H. Chen, *Ind. Eng. Chem. Res.*, 2011, **50**, 5942-5951.
33. H. R. Li, D. S. Zhang, P. Maitarad, L. Y. Shi, R. H. Gao, J. P. Zhang and W. G. Cao, *Chem. Commun.*, 2012, **48**, 10645-10647.
34. M. Kobayashi and K. Miyoshi, *Appl. Catal., B*, 2007, **72**, 253-261.
35. B. Pereda-Ayo, U. De La Torre, M. Romero-Sáez, A. Aranzabal, J. A. González-Marcos and J. R. González-Velasco, *Catal. Today*, 2013, **216**, 82-89.
36. J. X. Zhu, Z. Y. Yin, D. Yang, T. Sun, H. Yu, H. E. Hoster, H. H. Hng, H. Zhang and Q. Y. Yan, *Energy Environ. Sci.*, 2013, **6**, 987-993.
37. X. C. Jiang, T. Herricks and Y. N. Xia, *Nano Lett.*, 2002, **2**, 1333-1338.
38. S. X. Cai, D. S. Zhang, L. Y. Shi, J. Xu, L. Zhang, L. Huang, H. R. Li and J. P. Zhang, *Nanoscale*, 2014, **6**, 7346–7353.
39. V. P. Pakharukova, E. M. Moroz, V. V. Kriventsov, T. V. Larina, A. I. Boronin, L. Y. Dolgikh and P. E. Strizhak, *J. Phys. Chem. C*, 2009, **113**, 21368-21375.
40. C. C. Liu and H. S. Teng, *Appl. Catal., B*, 2005, **58**, 69-77.
41. H. L. Zhang, C. J. Tang, C. Z. Sun, L. Qi, F. Gao, L. Dong and Y. Chen, *Microporous Mesoporous Mater.*, 2012, **151**, 44-55.
42. S. Roy, B. Viswanath, M. S. Hegde and G. Madras, *J. Phys. Chem. C*, 2008, **112**, 6002-6012.
43. A. Gervasini, C. Messi, P. Carniti, A. Ponti, N. Ravasio and F. Zaccheria, *J. Catal.*, 2009, **262**, 224-234.
44. F. D. Liu, H. He, Y. Ding and C. B. Zhang, *Appl. Catal., B*, 2009, **93**, 194-204.
45. W. P. Shan, F. D. Liu, H. He, X. Y. Shi and C. B. Zhang, *Chem. Commun.*, 2011, **47**, 8046-8048.
46. Z. B. Wu, B. Q. Jiang, Y. Liu, H. Q. Wang and R. B. Jin, *Environ. Sci. Technol.*, 2007, **41**, 5812-5817.
47. D. L. Yuan, X. Y. Li, Q. D. Zhao, J. J. Zhao, M. Tade and S. M. Liu, *J. Catal.*, 2014, **309**, 268-279.
48. C. He, Y. K. Yu, L. Yue, N. L. Qiao, J. J. Li, Q. Shen, W. J. Yu, J. S. Chen and Z. P. Hao, *Appl. Catal., B*, 2014, **147**, 156-166.
49. D. S. Zhang, L. Zhang, L. Y. Shi, C. Fang, H. R. Li, R. H. Gao, L. Huang and J. P. Zhang, *Nanoscale*, 2013, **5**, 1127-1136.
50. F. Ayari, M. Mhamdi, J. Alvarez-Rodriguez, A. R. G. Ruiz, G. Delahay and A. Ghorbel, *Appl. Catal., B*, 2013, **134-135**, 367-380.
51. C. Fang, D. S. Zhang, L. Y. Shi, R. H. Gao, H. R. Li, L. P. Ye and J. P. Zhang, *Catal. Sci. Technol.*, 2013, **3**, 803-811.
52. L. Ma, Y. S. Cheng, G. Cavataio, R. W. McCabe, L. X. Fu and J. H. Li, *Appl. Catal., B*, 2014, **156-157**, 428-437.

53. R. D. Zhang, W. Yang, N. Luo, P. X. Li, Z. G. Lei and B. H. Chen, *Appl. Catal., B*, 2014, **146**, 94-104.
54. P. R. Ettireddy, N. Ettireddy, S. Mamedov, P. Boolchand and P. G. Smirniotis, *Appl. Catal., B*, 2007, **76**, 123-134.
55. P. P. Hu, Z. W. Huang, W. M. Hua, X. Gu and X. F. Tang, *Appl. Catal., A*, 2012, **437-438**, 139-148.
56. H. H. Phil, M. P. Reddy, P. A. Kumar, L. K. Ju and J. S. Hyo, *Appl. Catal., B*, 2008, **78**, 301-308.
57. N. Tang, Y. Liu, H. Q. Wang and Z. B. Wu, *J. Phys. Chem. C*, 2011, **115**, 8214-8220.
58. H. Z. Chang, X. Y. Chen, J. H. Li, L. Ma, C. Z. Wang, C. X. Liu, J. W. Schwank and J. M. Hao, *Environ. Sci. Technol.*, 2013, **47**, 5294-5301.
59. C. X. Liu, L. Chen, J. H. Li, L. Ma, H. Arandiyan, Y. Du, J. Y. Xu and J. M. Hao, *Environ. Sci. Technol.*, 2012, **46**, 6182-6189.
60. B. X. Shen, T. Liu, N. Zhao, X. Y. Yang and L. D. Deng, *J. Environ. Sci.*, 2010, **22**, 1447-1454.